NANO LETTERS

Letter

pubs.acs.org/NanoLett

Room-Temperature Micron-Scale Exciton Migration in a Stabilized Emissive Molecular Aggregate

Justin R. Caram,[†] Sandra Doria,[†] Dörthe M. Eisele,[§] Francesca S. Freyria,[†] Timothy S. Sinclair,[†] Patrick Rebentrost,[‡] Seth Lloyd,[‡] and Moungi G. Bawendi*[,†]

[†]Department of Chemistry and [‡]Department of Mechanical Engineering, Massachusetts Institute of Technology, Cambridge, Massachusetts 02139, United States

[§]Department of Chemistry and Biochemistry, Center for Discovery and Innovation, The City College of New York of The City University of New York, 160 Convent Avenue, New York, New York 10031 United States

S *Supporting Information*

ABSTRACT: We report 1.6 ± 1 μm exciton transport in self-assembled supramolecular light-harvesting nanotubes (LHNs) assembled from amphiphillic cyanine dyes. We stabilize LHNs in a sucrose glass matrix, greatly reducing light and oxidative damage and allowing the observation of exciton−exciton annihilation signatures under weak excitation flux. Fitting to a one-dimensional diffusion model, we find an average exciton diffusion constant of 55 ± 20 cm^2/s, among the highest measured for an organic system. We develop a simple model that uses cryogenic measurements of static and dynamic energetic disorder to estimate a diffusion constant of 32 cm^2/s, in agreement with experiment. We ascribe large exciton diffusion lengths to low static and dynamic energetic disorder in LHNs. We argue that matrix-stabilized LHNS represent an excellent model system to study coherent excitonic transport.

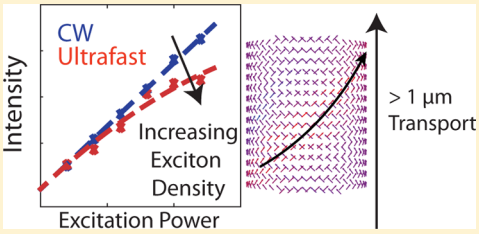

KEYWORDS: *J-aggregate, molecular aggregate, exciton, exciton diffusion, coherent exciton, exciton delocalization*

Excitons are bound electron−hole pairs generated upon absorption of a photon or through charge carrier injection. Photosynthetic organisms and organic electronics make use of ordered molecular aggregates as excitonic antennas, with energy transport out-competing radiative and nonradiative decay channels leading to near-unity internal quantum efficiencies.[1,2] Like electronic conduction, molecular exciton conduction falls largely in two regimes: hopping and delocalization. In the hopping regime, interaction with the environment (the reorganization energy) exceeds the dipole−dipole coupling ($\lambda_{reorg} > J$), leading to Forster resonance dominated transport. In the delocalized regime, dipole−dipole coupling exceeds the reorganization energy leading to Redfield transport.[3,4] Efficient conduction of spin-singlet excitons requires a balance of these two regimes, with both coherent quantum delocalization and incoherent resonance energy transfer playing a role in natural and artificial light-harvesting systems.[3,5−7] However, extracting principles of design from disordered complex biological and polymer systems is a significant challenge.[8] This study probes singlet exciton transport in self-assembled light harvesting nanotubes (LHNs). LHNs are quasi one-dimensional J-aggregates consisting of ordered amphiphillic cyanine dyes that form extended transition dipoles with concentrated oscillator strength in a lower-energy, highly emissive state.[9] LHNs show remarkably high overall coupling, negligible reorganization energies, and high structural uniformity resulting in large delocalization lengths. LHNs are an excellent model material for exploring the relationship between quantum delocalization and energy transport in a system where $\lambda_{reorg} \ll J$ (coherent regime).[10−12] However, spectroscopic studies of LHNs have been hampered by difficulties in sample preparation[13] and photoinstability.[14] As a result, studies of exciton transport in LHNs have yielded highly variable results,[15−17] with estimates of transport ranging from 30 to 300 nm at room temperature and even 25 μm at 5K.

This study is divided into two parts. In the first section, we demonstrate matrix-stabilization of LHNs and use exciton−exciton annihilation to estimate exciton diffusion lengths and constants. In the second section, we use the measurements of energetic disorder and simulations of exciton delocalization to model exciton diffusion and compare this to the experimental results. We begin the first section by characterizing LHNs prepared in a sucrose−trehalose solid matrix that prevents photoxidative damage and allows for detailed spectroscopic characterization. We then probe signatures of exciton−exciton annihilation (EEA) by comparing ultrafast and continuous wave laser excitations at the same powers and wavelength. We show that both photoluminescent lifetimes and relative quantum yields of LHNs are strongly mitigated by EEA and fit our results to a diffusive model to estimate exciton transport. Measurements of EEA are found to be consistent with exciton diffusion lengths in excess of 1 μm over multiple measurements and samples. In the second section, we begin by examining

Received: June 20, 2016
Revised: September 8, 2016

DOI: 10.1021/acs.nanolett.6b02529
Nano Lett. XXXX, XXX, XXX−XXX

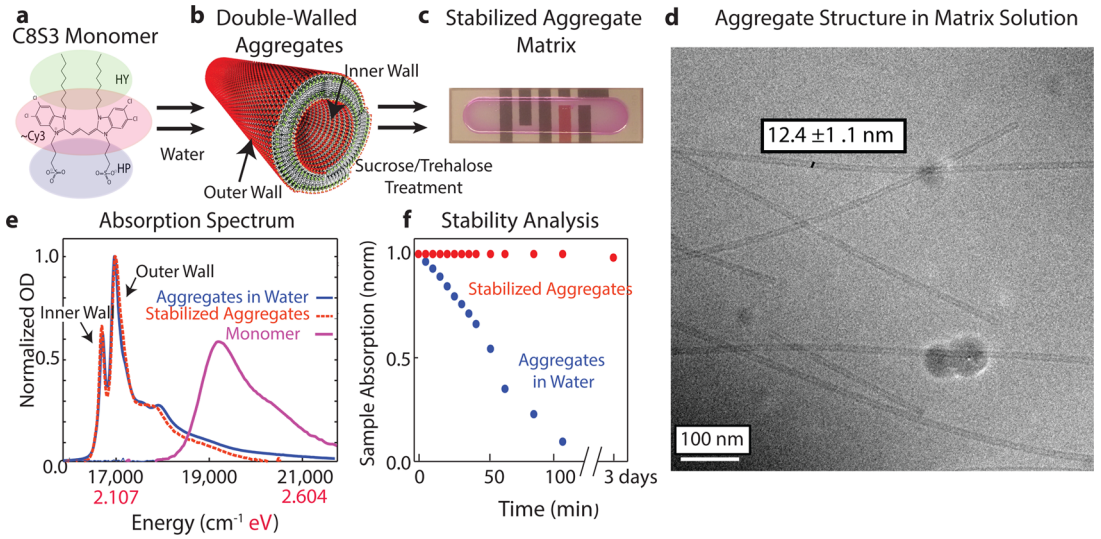

Figure 1. (a) Self-assembly of amphiphillic C8S3 monomers with hydrophobic, carbocyanine dye and hydrophilic moieties in a water−methanol solution into (b) double-walled tubular light-harvesting nanotubes. (c) LHNs are stabilized in a dry inert sucrose−trehalose clear glass matrix. (d) Cryo-EM of LHNs in matrix retain double wall character with 12.5 nm outer wall and μms of longitudinal extent. (e) The absorption spectrum of C8S3 in methanol red shifts and narrows with respect to the monomer upon addition of water when aggregates are formed, with distinct features corresponding to inner- and outer-wall subsystems. LHNs suspended in a sugar matrix retains aggregate spectral character. (f) Plotting the normalized intensity of absorption over several days shows rapid degradation of LHNs under room light, and the matrix-stabilized LHNs retain spectral integrity over days.

temperature-dependent fluorescent and absorption line widths, from which we extract static and dynamic energetic disorder of LHNs. From this disorder and calculations of exciton delocalization length and direction, we simulate partially coherent exciton propagation to find diffusion constants. We find that both experimental EEA and disorder model-based estimates of exciton propagation give similar results for diffusion constants, 55 versus 32 cm^2/s. We close by comparing LHNs to other excitonic antennas and discuss how exciton propagation may be controlled through the selective introduction of disorder.

Stabilization of LHNs. We form LHNs from 3,3′-bis(2-sulfopropyl)- 5,5′,6,6′-tetrachloro-1,1′- dioctylbenzimidacarbocyanine (C8S3) molecules that self-assemble in a water−methanol mixture into a well-defined double-walled nested cylindrical morphology, characterized previously via complementary spectroscopy, microscopy, and electronic structure modeling.[10,13,16,18] C8S3 dye monomers consist of three structural moieties, a hydrophobic alkyl group, a carbocyanine dye (similar to Cy3), and a hydrophilic charged sulfonate tail (Figure 1a). In a water−methanol mixture, C8S3 monomers self-assemble into nanotubes with an outer wall diameter of ∼12.5 nm, an inner wall diameter of ∼6 nm, and longitudinal dimensions tens of micrometers in length (panels b and d of Figure 1).[13,16]

To accomplish our study, we have developed a method to stabilize C8S3 LHNs against light-induced and cryogenic damage in a sugar-based matrix.[19] We modify the normal preparation by diluting the aggregate preparation in a highly concentrated sucrose−trehalose solution and drying overnight to create a concentrated, clear, dry, sugar-glass matrix (Figure 1c). Figure 1d shows that matrix preserved LHNs have identical macroscopic structural features under cryo-electron microscopy. In Figure 1e, we plot the absorption of C8S3 dye molecules in methanol, C8S3 LHNs in a water−methanol mixture, and LHNs embedded in the solid sugar matrix. Spectral features unique to the inner wall (16 700 cm^{-1}) and outer wall (17 000 cm^{-1}) subsystems are maintained upon water removal in the matrix.[10] Matrix-suspended LHNs are photostable over several days under ambient room light and in air (Figure 1f), enabling temperature-dependent linear and transient optical spectroscopies.

Measurements of Exciton−Exciton Annihilation. To quantify exciton motion in LHNs we monitor ultrafast laser-induced exciton−exciton annihilation (EEA) in Figures 2 and 3. In Figure 2a, we show fluorescence spectra of LHNS taken with both continuous wave (CW) and ultrafast excitation at the same power and wavelength. While spectral features are maintained, we observe a decrease in the relative quantum yield in the latter case. In Figure 2b we demonstrate that integrated fluorescence under CW excitation is linear with incident power, while ultrafast excitation shows a quadratic decrease in the integrated intensity. Ultrafast excitation impulsively generates a high initial density of temporally and spatially coincident excitons on LHNs, which can diffuse, radiatively and nonradiatively decay, and overlap and collide. When these excitons interact, they annihilate leading to a decrease in overall quantum yield. Therefore, EEA is a spectroscopic signature that probes the dimensionality, distance, and domain size of exciton diffusion.[20] In Figure 2, in red, we estimate the number of excitations per unit aggregate for each incident ultrafast laser pulse. Assuming a uniform intensity over the beam waist the initial exciton density per unit distance of aggregate is the number of excitation events per pulse divided by the number of molecules in the focal volume and the effective longitudinal distance of aggregate per molecule. The equation is as follows:

$$\eta_0 = \underbrace{\left(\frac{\chi\lambda_{exc}(1-10^{-OD_{exc}})}{hc}\right)}_{\text{number of excitations}}\underbrace{\left(\frac{OD_{max}\pi R_b^2}{\epsilon_{max}}\right)^{-1}}_{\text{focal concentration}}\underbrace{(a_0)^{-1}}_{\text{molecular distance}} \quad (1)$$

DOI: 10.1021/acs.nanolett.6b02529
Nano Lett. XXXX, XXX, XXX−XXX

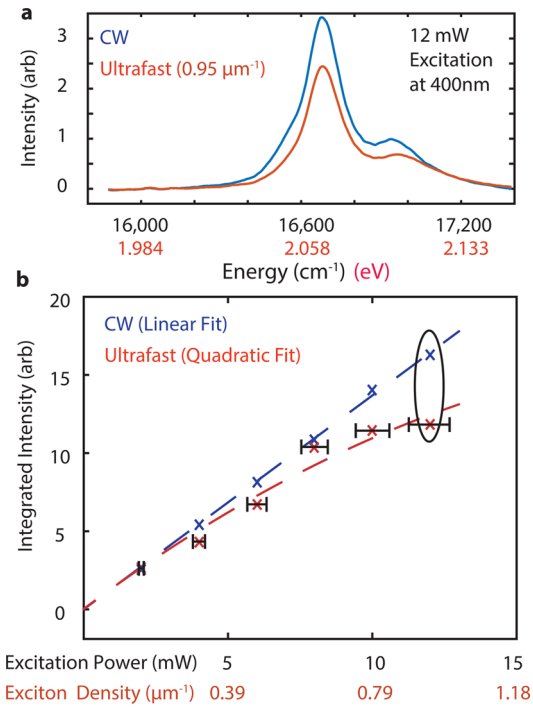

Figure 2. (a) Fluorescence spectrum for both continuous wave (CW) and ultrafast laser excitation at 12 mW. We observe a clear decrease in PL intensity due to EEA upon ultrafast excitation. (b) Integrated fluorescence intensity for both CW and ultrafast excitation. For ultrafast excitation, we include an estimate of initial exciton density calculated using eq 1, with error propagated from experimental uncertainty. Lines represent a linear (CW) or quadratic (ultrafast) fit to the data, demonstrating clear signatures of EEA at low interexciton average distances.

where χ is the pulse energy, R_b is the radius of excitation, $OD_{exc/max}$ is the optical density at the excitation or absorption maximum, λ is the wavelength of excitation, hc is Planck's constant and the speed of light, ϵ the molar absorptivity, and a_0 is the linear displacement per monomer along the primary access of the aggregate (including inner and outer walls). Table 1 gives estimates for all of these parameters. In Figure 2, we show estimates of initial exciton density in red and find in Figure 2b EEA signatures at very low average interexciton distances (<0.1 μm^{-1}).

In Figure 3, we relate measurements of EEA to empirical estimates of exciton diffusion lengths and constants. To model signatures of EEA, we apply a model that assumes diffusive site-to-site transport of excitons. In this case, excitons are impulsively generated and undergo an unbiased random walk, annihilating on contact (Figure 3a,b). Using a Monte Carlo simulation shown in Figures 3b–d, we model the spectroscopic signatures of EEA: time-resolved photoluminescence lifetime (PL) and relative quantum yield (QY). In our model, excitons are randomly distributed and propagate until they either decay (according to first-order kinetics) or annihilate. We use a one-dimensional exciton diffusion model due to the large aspect ratio of LHNs (12.5 versus >500 nm), which argues that exciton motion will mostly be along the primary axis of the aggregate. We vary the initial exciton density and monitor the total population at each time step (PL in Figure 3c), counting the number of decayed excitons (QY in Figure 3d). Increasing exciton density most clearly manifests in the initial time period of the PL and suppresses the relative QY. We can also model exciton dynamics analytically using the governing kinetic equation:

$$\frac{d(\eta(t))}{dt} = -\eta(t)/t_{tot} - \frac{\beta}{\sqrt{t}}\eta(t)^2 \quad (2)$$

$$\eta(0) = \eta_0 \quad (3)$$

where $\eta(t)$ and η_0 represent the time-dependent and initial exciton density, t_{tot} represents the total exciton lifetime due to first-order decay processes (radiative and nonradiative) and β can be related to the root-mean-square exciton displacement ($\beta = \sqrt{\frac{\langle x^2 \rangle}{\pi t_{tot}}} = \sqrt{2D/\pi}$). We motivate the assumptions in this equation and solve for η (t) in the Supporting Information. Figure 3e shows the resulting PL estimates under different initial exciton densities. Figure 3f plots the relative QY, which we arrive at by numerically integrating $\int_0^\infty \eta(t)/\eta_0 dt$.

In Figure 3g,h we plot the experimental PL and relative QY from 520 nm ultrafast excitation (where the aggregates absorb ~10% of the incoming light). We fit the normalized PL and the relative QY to $\eta(t)$ to find β, from which we can arrive at diffusion constant and diffusion length estimates. In four aggregate preparations, characteristic signatures of EEA were observed at photon fluxes as low as 0.01 excitations/μm of LHN with 520 nm excitation. Our fits of both PL (one trial) and QY (three trials) yielded diffusion constants of 55 ± 20 cm^2/s and exciton diffusion lengths along the longitudinal dimension of the aggregate of 1.6 ± 1 μm at room temperature. We observe a constant offset in the PL, which we assign to aggregates not participating in EEA. In Figure S4, we quantify the size-distribution of aggregates. From this, we estimate that 80% of aggregates do not participate in EEA at 0.5 excitations per micrometer due to shorter aggregate length scales (see the Supporting Information).

Modeling Exciton Motion from Measurements of Static and Dynamic Disorder. In this section, we use a different approach to estimate exciton diffusion using measurements of static (inhomogeneous) and dynamic (homogeneous) energetic disorder. Exciton motion can be characterized as falling in two regimes. If both static and dynamic disorder is high, the exciton interacts with the environment prior to full delocalization. In this regime, energy moves through FRET transfer from dipole to dipole. In materials with low static and dynamic disorder, coherent delocalization can occur prior to interactions with the local environment, leading to Redfield transport. Low energetic disorder in LHNs leads to coherent delocalization of at least 40 monomer units at room temperature.[10] We thus assume exciton transport occurs in the Redfield limit, at which point transfer is mediated by the interaction with the environment. To summarize our approach, we use temperature-dependent absorption and emission line widths to estimate the time-scales of exciton delocalization and environmentally induced dephasing. We then use a Frenkel exciton Hamiltonian to determine the total coupling and the direction of exciton delocalization. Using a Monte Carlo simulation, we allow excitons to ballistically delocalize along this axis with a speed set by the total coupling and a step time set by environment mediated localization, derived from the homogeneous line width. From this MC simulation, we determine an exciton diffusion constant and compare it to the experimentally measured value.

DOI: 10.1021/acs.nanolett.6b02529
Nano Lett. XXXX, XXX, XXX−XXX

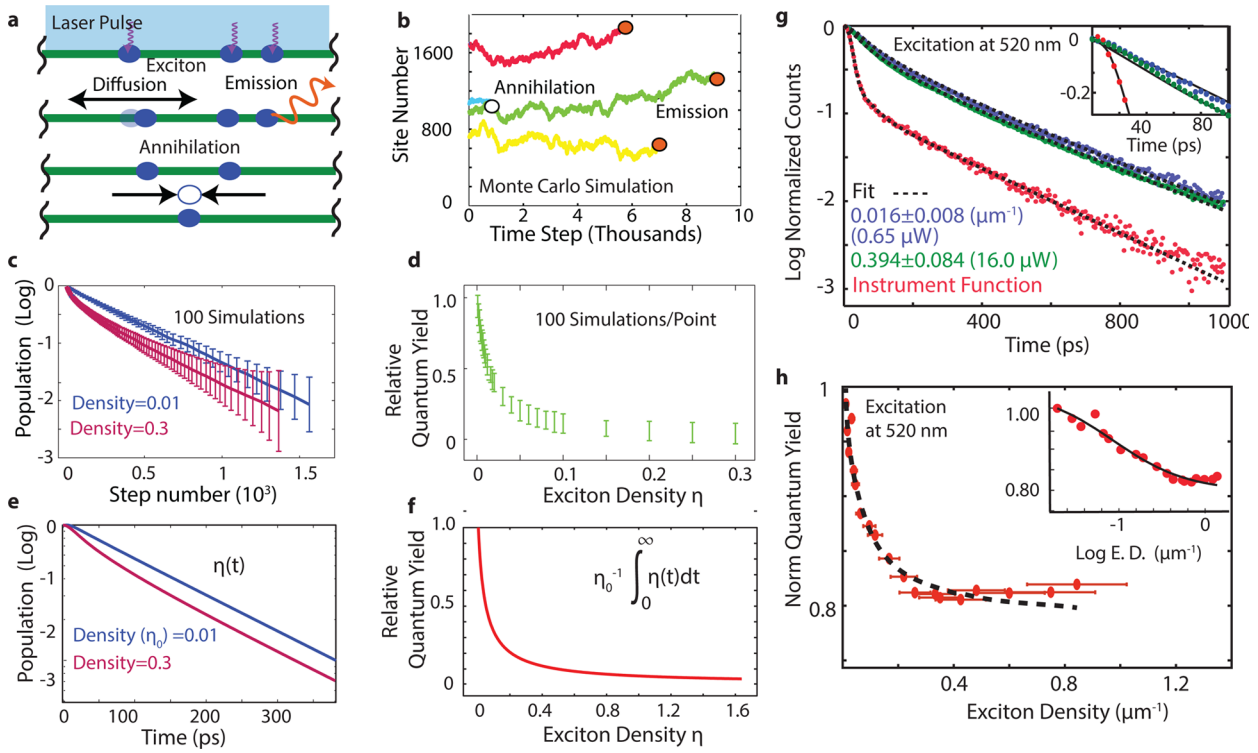

Figure 3. (a) Ultrafast laser pulse generation of excitons along a linear chain. These excitons can diffuse or annihilate, as seen in exciton trajectories shown in (b) from Monte Carlo simulations. (c) The population of excitons at each time step (PL) and (d) the relative number of decayed excitons (relative QY) are plotted as a function of initial exciton density. The solution to the diffusive EEA model (eq 2) is plotted in (e), showing the PL and numerically integrated in (f) for the relative QY for high and low exciton density. We qualitatively show the agreement of the diffusive model with MC simulation. (g) Experimental PL lifetimes at low (blue) and high (green) excitation flux are consistent with the model of diffusive EEA (plotted in black). We plot the instrument response in red. The inset displays early time behavior. (h) The relative quantum yield is plotted on a linear/(log) excitation scale (inset). We fit using the result the solution of eq 2 further described in the Supporting Information, with our fit plotted in black. We observe a constant offset that we assign to noncontributing finite domains that do not participate in EEA (described further in Figure S4).

Table 1. Parameters Used to Determine Exciton Density in Eq 1 and Plotted in Both Figures 2 and 3

parameters	
χ_{400}	12.5−500 ± 0.13 pJ
χ_{520}	1.25−500 ± 0.13 fJ
OD_{400}	0.001 ± 0.0005
OD_{520}	0.115 ± 0.001
OD_{max}	0.920 ± 0.001
$R_{b_{400}}$	30 ± 1 μm
$R_{b_{520}}$	20 ± 1 μm
a_0	0.0247 nm/molecule
ϵ_{max}	(5.55 ± 0.02) × 10^5 M^{-1} cm^{-1}

In Figure 4a,b, we show temperature-dependent absorption and emission spectra, which we use to quantify sources of line broadening. As Figure 4a shows, we observe significant narrowing of inner and outer wall features as temperature is decreased from 298 to 77 K and continuing to 5 K (Figure S1), in direct contrast to previous cryogenic studies of aggregates stabilized in poly(vinyl alcohol), which show no line-width change.[21] This is clear evidence that matrix preserved aggregates have decreased inhomogeneous line widths, which enables the observation of the temperature-dependent homogeneous line-narrowing. The relative peak ratio between outer-wall (OW) and inner-wall (IW) emission follows a Boltzmann distribution in agreement with two weakly coupled electronic subsystems at thermal equilibrium (see the Supporting Information).[21] In Figure 4a, we fit the inner-wall feature to the convolution of Gaussian and Lorentzian lineshapes (a Voight function) described in more detail in the Supporting Information. We fix the Gaussian line width and vary only the Lorentzian width at each temperature. In Figure 4b, we plot the Voight function full-width half-maximum (fwhm) from a typical preparation of LHNs. Absorption and emission line widths track closely and are highly reproducible (see the Supporting Information). Comparing absorption and emission, we find that LHNs show little to no Stokes shift for emission from the inner wall for all temperatures. Little Stokes shift suggests weak coupling to the local environment and few low-energy traps, motivating our treatment of exciton diffusion as an unbiased random walk.

In condensed-phase electronic transitions, line broadening and Stokes shift arise from both temperature-dependent interactions, such as intra- and intermolecular vibrations and solvent reorganization, and temperature-independent static disorders, such as local environmental, chemical, and structural heterogeneity. From the temperature-independent term of the Voight function fit, we estimate the contribution of static energetic disorder to be 115 cm^{-1} (fwhm), roughly half of previous reports for this system,[10,18] close to the average absorption and emission line width at 5 K. The room temperature line width is the convolution of this static Gaussian line width with the temperature-dependent Lorentzian line width. Using repeated measurements, we find the Lorentzian homogeneous fwhm to be 118 cm^{-1} at 298 K.

DOI: 10.1021/acs.nanolett.6b02529
Nano Lett. XXXX, XXX, XXX−XXX

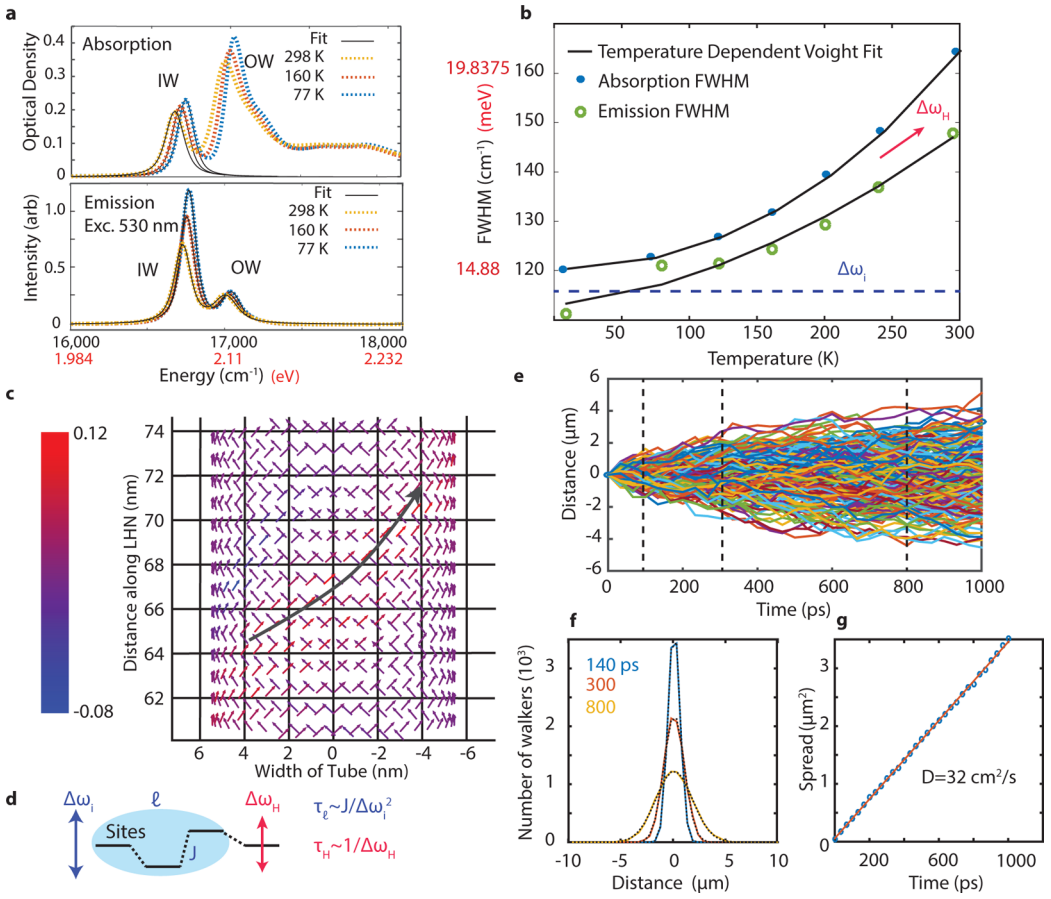

Figure 4. (a) Temperature-dependent absorption and emission spectra fit to a Voight profile, with inner-wall (IW) and outer-wall (OW) features highlighted. (b) Emission and absorption line widths for the inner wall plotted with a power law overlay, as described in the Supporting Information. The low-energy line width represents average static inhomogeneous line broadening. (c) The eigenvalues of an exciton from the main parallel transition modeled using the geometric parameters from ref 18. The exciton propagates along the direction of highest coupling with a pitch of 49.1°. (d) One-dimensional unbiased exciton transport can be described using a three-parameter model that includes site−site coupling, static energetic disorder, and dynamic energetic disorder (J, ω_I, and ω_H, respectively). J and ω_I determine the delocalization time (t_l) and length (l), while ω_H sets the interaction time scale (t_H). (e) A Monte Carlo simulation of exciton trajectories, with t_H t_l specified in parts a and b. (f) The exciton spread measured from each trajectory is used to extract RMS diffusion, which in turn is fit to a line (g) to determine the diffusion constant.

Homogeneous line broadening dephases (or decoheres) the phase relationship between the excited-state and ground-state wave function and thus reflects interactions of the system with its bath that localized the excitation. This localization comes from transitions between eigenstates of the system Hamiltonian, which also serve to move the exciton center of mass. We note that the negligible Stokes shift and Lorentzian line width suggest weak coupling to a continuum of low-frequency modes leading to pure dephasing of the electronic transition.[22] In Figure 4b, we plot the temperature dependence of the line width varying the Lorentzian component according to a power law $a_H T^n$, with $n = 2 \pm 0.5$, also consistent with models of pure electronic dephasing for molecular aggregates.[23]

In Figure 4c−g, we apply a coarse grain model that uses the aggregate Hamiltonian and measurements of static and dynamic disorder to estimate exciton diffusion constants. We fully derive this model in the Supporting Information following reference 24. To summarize our approach, we use the coupling between sites to estimate the speed of exciton delocalization and use the homogeneous line width to estimate the time scale on which the exciton center of mass moves. The direction of propagation is randomized upon each step, creating dynamic unbiased random walk. To start, using prior structural models,[18] we create a site Hamiltonian with 6000 site energies centered at 18 868 cm^{-1} with a distribution of 600 cm^{-1}, creating an aggregate with longitudinal dimension of ∼140 nm, shown in Figure S3. We estimate coupling (off-diagonal elements) using an extended dipole approximation.[25] We diagonalize the site Hamiltonian and plot the wave function coefficients of each site for a typical exciton, whose energy is in the primary parallel aggregate transition (Figure 4c). As can be seen, the exciton delocalizes helically along the primary axis of the nanotube and over several consecutive rings, with a pitch of 49.1° relative to the longitudinal axis of the aggregate. This is the direction of delocalization and thus the fastest coherent propagation, and we use this to arrive at a per-monomer exciton displacement of 1.03 nm.

To model the dynamics along this axis, we use three parameters shown in Figure 4d. J, ω_I, and ω_H are defined as the site−site coupling, static energetic disorder and dynamic energetic disorder, respectively. In this model, the exciton propagates ballistically with a velocity of $2J$ until it either reaches its delocalized extent, l on the time scale tt_l, or it interacts with the environment on the time-scale t_H. If it reaches its delocalized extent, the step size is set by $l = 2Jt_l = 4\pi^2J^2/\Delta\omega_I^2$. If it interacts with the environment first, the step size is

DOI: 10.1021/acs.nanolett.6b02529
Nano Lett. XXXX, XXX, XXX−XXX

$2Jt_H = 2J/\omega_H$ (for Lorentzian homogeneous broadening). The number of steps taken by an exciton undergoing a random walk is the exciton lifetime (t_{tot}) divided by the time scale of interaction with the environment t_H, which makes the root-mean-square longitudinal diffusion length $x_{rms} = 2Jt_x\sqrt{t_{tot}/t_H}$ where $x = l$ if $t_l < t_H$ and $x = H$ if $t_l > t_H$. Either the system fully delocalizes before hopping or its delocalization is limited by the interaction with the environment. We note that this model is qualitatively similar to Redfield theory, in which transport is mediated by a perturbative interaction by the local environment.[26]

From our measurements, we find $t_H \ll t_l$ (900 fs versus 30 ps) leading to mostly coherent propagation of excitons punctuated by steps induced by interactions with the local environment. We use a Monte Carlo simulation to extract diffusion constants from our estimates of J, ω_l, and ω_H assuming transport proceeds along the helical turn in the direction of strongest J-coupling. In Figure 4e, we generate a set of trajectories by randomly drawing Poisson distributed interaction times with characteristic time scale, t_H, and set the step size by how far it can propagate during that time. In Figure 4f, we histogram the final positions of each exciton and fit it to a Gaussian distribution. The square of the exciton spread (the Gaussian standard deviation) is then fit to a line to extract a diffusion constant. We use measured values of $\omega_l = 57$ cm^{-1} and $\omega_H = 115$ cm^{-1} and a theoretical derived exciton coupling, $J \approx -688$ cm^{-1}. We estimate J from the total coupling in the model used to produce Figure 4c.[27] From this approach, we find a linear diffusion constant of 32 cm^2/s within the range of the measured value of 55 ± 20 cm^2/s.

The agreement between measurement and disorder-based estimates of exciton diffusion argues that long-range exciton migration is a natural result of high coupling and low static disorder in LHNs. Low static disorder allows for partially coherent exciton propagation that is only slowed by interactions with the environment, which serves to localize the excitation, while high coupling increases the speed and length scale of quasi-ballistic delocalization. This model, however, does not account for super-radiant resonant energy transfer through FRET between highly delocalized states.[28] Delocalization enhances transport by additively increasing the number of dipole−dipole interactions. However, the PL lifetime dynamics of long-range direct annihilation has the same functional form as one-dimensional exciton−exciton annihilation, making it a challenge to asses this alternative mechanism.[29] A more-sophisticated model of quantum transport including both super-radiance and coherence may account improve the agreement between theory and experiment.

Comparison to Other Excitonic Antenna and Conclusions. Room-temperature macroscopic exciton propagation (>1 μm) is a rare phenomenon in organic systems. Organic semiconductors such as poly(3-hexylthiophene) (P3HT) and PTCDA also form J-aggregates yet transport excitons only approximately tens of nanometers before trapping,[29,30] with diffusion constants 4 orders of magnitude lower than those of LHNs ($D \approx 10^{-3}$ cm^2/s). Interestingly, LHNs have nearly identical diffusion constants to those of vacuum-suspended uniform carbon nanotubes (CNTs) ($D \approx 45$ cm^2/s),[31] although CNT exciton propagation decreases significantly in solution due to the introduction of trap states.[32] Recently reported carbonyl-bridged triarylamine linear molecular aggregates display micron-scale diffusion, seemingly limited only by the domain size of the material.[33] The observed length scale of exciton diffusion is aided by long lifetimes due to symmetry forbidden radiative channels (as an H-type aggregates). This is analogous to long-range triplet exciton diffusion in pentacene and tetracene materials, also assisted by forbidden exciton recombination.[34] Interestingly, we observe similar exciton diffusion lengths despite far-shorter excited-state lifetimes, leading to significantly larger diffusion constants. Therefore, long-lifetimes are not a strict prerequisite for long-distance exciton transport in the condensed phase.

We find that LHNs in an ordered, glassy matrix display micron-scale exciton diffusion lengths. We are able to reproduce large diffusion constants using a disorder-based model, which suggests that large coupling and low-static disorder are critically important for long-range exciton transport. J-aggregates have already been used as materials to enhance absorption in devices through coupling to inorganic nanomaterials.[35,36] Stabilized LHNs can thus act as quasi-one-dimensional excitonic wires for energy conduction. Furthermore, if conduction is mostly coherent, control of temperature and local energetic disorder can be used to modulate exciton migration. Exploring how energetic disorder controls exciton transport may be an interesting avenue for future research.

Methods. *Sample Preparation.* To prepare the aggregate, we follow the "alcoholic" route,[37] modifying it slightly to create the high-concentration sugar glass. A total of 260 μL of 2.92 mM C8S3 monomer (FEW chemicals) in methanol are mixed with 1 mL of deionized water and allowed to sit overnight. We then mix 100 μL of aggregate solution with a 100 μL of a saturated solution of 50% sucrose and 50% trehalose by weight (Sigma). We deposit the sugar aggregate mixture onto a 0.2 mm path length quartz cuvette (Starna), forming a neat thick film. We then place the cuvette under vacuum (0.5 atm) for 24 h, removing water and drying into a uniform amorphous glass (Figure 1c). Using the sugar glass as a cryoprotectant, we perform low-temperature absorption (Cary UV−vis) and emission (Horiba Jobin Yvon Fluoromax) spectroscopy in a coldfinger cryostat (Janis ST-100). Cryosamples were prepared by dropping ∼5 μL of LHN sugar solution matrix on lacey grids coated with a continuous carbon film (Lacey Formvar Stabilized with Carbon, 200 mesh). Before using, the copper grids were hydrophilized by an oxygen plasma treatment for 10 s, performed with a Salaries Advanced Plasma cleaning system, Gatan Inc. To remove sample in excess without damaging the carbon layer, the grids were blotted in a Gatan Cryo Plunge III. The samples were quickly plunged into liquid ethane to make very thin vitrified layer. The temperature of plunging workstation was set with −175 °C. The grids were mounted on a Gatan 626 single tilt cryoholder equipped in the TEM column. The specimen and the holder tip were cooled by liquid nitrogen, which is maintained during transfer into the microscope and subsequent imaging. The imaging was performed with an JEOL 2100 FEG microscope operated at 200 kV and a magnification in the range of 10 000×−60 000×. All images were recorded on a Gatan 2k × 2k UltraScan CCD camera.

Exciton−Exciton Annihilation Measurement. Using either the doubled 400 nm output of Ti:S oscillator (Coherent, Mira) or 300 fs laser pulse centered at 520 nm (Toptica Femtofibre TVIS 80 MHz), we impulsively generate a population of excitons that fully relaxes to the ground state prior to re-excitation (lifetime of 300 ps versus 12.5 ns). We use a power meter (Thorlabs) to estimate the initial exciton density and

DOI: 10.1021/acs.nanolett.6b02529
Nano Lett. XXXX, XXX, XXX−XXX

monitor the population of excitons using a single-photon-counting avalanche photodiode (Micro Photon Devices) and time correlated single photon counter with a time resolution of 4 ps (Picoquant PicoHarp). We collect an instrument response function by reflecting the laser directly onto the detector (fwhm 40 ps). We monitor the relative quantum yield of the aggregate glass by measuring the power and collecting the spectra simultaneously (Ocean Optics spectrometer). We measure the size of our excitation using a USB camera. At fluxes above 40 nJ/cm^2, we observe slow reversible photobleaching of the sample. To avoid this, after each spectral collection, the sample is translated 100 μm, and we only consider data taken below that fluence. All analysis and fitting is done in MATLAB.

■ ASSOCIATED CONTENT

Supporting Information

The Supporting Information is available free of charge on the ACS Publications website at DOI: 10.1021/acs.nanolett.6b02529.

Additional details on modeling, simulating, and measuring exciton annihilation. Figures showing typical absorption and emission spectra from all temperatures, full width half max for four sets of temperature-dependent experiments, inner and outer wall peak ratios follow a Boltzmann distribution, lifetime and quantum yield increases, the experimental setup for studying EEA, a plot of PL intensity under continuous excitation at 530 nm, an estimate of the number of aggregates that can participate in EEA as a function of excitation density and length of aggregate, a plot of the stick spectrum of the dipole weighted eigenvalues of a single aggregate Hamiltonian with 600 cm^{-1} of diagonal disorder, and a plot of exciton wavefunction. Tables showing fit parameters obtained with the model in eq S9 for the absorption and emission spectra and from eq S11 in different temperature-dependent experiments. (PDF)

■ AUTHOR INFORMATION

Corresponding Author

*E-mail: mgb@mit.edu.

Notes

The authors declare no competing financial interest.

■ ACKNOWLEDGMENTS

This work was supported by Eni SpA under the Eni-MIT Alliance Solar Frontiers Center. D.M.E. and J.R.C. were funded in part by the Department of Energy (DOE) through the DOE Center for Excitonics (an Energy Frontiers Research Center funded by the U.S. DOE, Office of Science, Office of Basic Energy Sciences, through grant no. DE-SC0001088). D.M.E. also acknowledges the Alexander von Humboldt Foundation, the Research Foundation of the City University of New York (CUNY), and the Martin and Michelle Cohen Fund for Science.

■ REFERENCES

(1) Blankenship, R. E. *Molecular Mechanisms of Photosynthesis*; Blackwell Science Ltd: Williston, VT, 2002.

(2) Park, S. H.; Roy, A.; Beaupre, S.; Cho, S.; Coates, N.; Moon, J. S.; Moses, D.; Leclerc, M.; Lee, K.; Heeger, A. J. *Nat. Photonics* **2009**, *3*, 297−302.

(3) Cao, J.; Silbey, R. J. *J. Phys. Chem. A* **2009**, *113*, 13825−13838.

(4) Ishizaki, A.; Fleming, G. R. *Proc. Natl. Acad. Sci. U. S. A.* **2009**, *106*, 17255−17260.

(5) Engel, G. S.; Calhoun, T. R.; Read, E. L.; Ahn, T.-K.; Mancal, T.; Cheng, Y.-C.; Blankenship, R. E.; Fleming, G. R. *Nature* **2007**, *446*, 782−786.

(6) Mohseni, M.; Rebentrost, P.; Lloyd, S.; Aspuru-Guzik, A. *J. Chem. Phys.* **2008**, *129*, 174106.

(7) Chin, A. W.; Datta, A.; Caruso, F.; Huelga, S. F.; Plenio, M. B. *New J. Phys.* **2010**, *12*, 115002.

(8) Scholes, G. D.; Rumbles, G. *Nat. Mater.* **2006**, *5*, 683−696.

(9) Jelley, E. E. *Nature* **1936**, *138*, 1009−1010.

(10) Eisele, D. M.; Cone, C. W.; Bloemsma, E. A.; Vlaming, S. M.; van der Kwaak, C. G. F.; Silbey, R. J.; Bawendi, M. G.; Knoester, J.; Rabe, J. P.; Vanden Bout, D. A. *Nat. Chem.* **2012**, *4*, 655−662.

(11) Yuen-Zhou, J.; Arias, D. H.; Eisele, D. M.; Steiner, C. P.; Krich, J. J.; Bawendi, M. G.; Nelson, K. A.; Aspuru-Guzik, A. *ACS Nano* **2014**, *8*, 5527−5534.

(12) Lim, J.; Palecek, D.; Caycedo-Soler, F.; Lincoln, C. N.; Prior, J.; von Berlepsch, H.; Huelga, S. F.; Plenio, M. B.; Zigmantas, D.; Hauer, J. *Nat. Commun.* **2015**, *6*, 7755−7760.

(13) Eisele, D. M.; Arias, D. H.; Fu, X.; Bloemsma, E. A.; Steiner, C. P.; Jensen, R. A.; Rebentrost, P.; Eisele, H.; Tokmakoff, A.; Lloyd, S.; Nelson, K. A.; Nicastro, D.; Knoester, J.; Bawendi, M. G. *Proc. Natl. Acad. Sci. U. S. A.* **2014**, *111*, E3367−E3375.

(14) Lyon, J. L. L.; Eisele, D.; Kirstein, S.; Rabe, J. P.; Vanden Bout, D. A.; Stevenson, K. J. *ECS Trans.* **2008**, *16*, 77−84.

(15) Spitz, C.; Daehne, S. *Int. J. Photoenergy* **2006**, *2006*, 84950−84957.

(16) Eisele, D. M.; Knoester, J.; Kirstein, S.; Rabe, J. P.; Vanden Bout, D. A. *Nat. Nanotechnol.* **2009**, *4*, 658−663.

(17) Clark, K. A.; Krueger, E. L.; Vanden Bout, D. A. *J. Phys. Chem. Lett.* **2014**, *5*, 2274−2282.

(18) Didraga, C.; Pugžlys, A.; Hania, P. R.; von Berlepsch, H.; Duppen, K.; Knoester, J. *J. Phys. Chem. B* **2004**, *108*, 14976−14985.

(19) Wright, W. W.; Carlos Baez, J.; Vanderkooi, J. M. *Anal. Biochem.* **2002**, *307*, 167−172.

(20) Paillotin, G.; Swenberg, C. E.; Breton, J.; Geacintov, N. E. *Biophys. J.* **1979**, *25*, 513−533.

(21) Clark, K. A.; Krueger, E. L.; Vanden Bout, D. A. *J. Phys. Chem. C* **2014**, *118*, 24325−24334.

(22) Mukamel, S. *Principles of Nonlinear Optical Spectroscopy*; Oxford: London, 1999.

(23) Heijs, D. J.; Malyshev, V. A.; Knoester, J. *J. Chem. Phys.* **2005**, *123*, 144507.

(24) Lloyd, S.; Mohseni, M.; Shabani, A.; Rabitz, H. 2011, arXiv:1111.4982. arXiv.org e-Print archive. https://arxiv.org/abs/1111.4982 (accessed Feb 1, 2016).

(25) Czikklely, V.; Forsterling, H. D.; Kuhn, H. *Chem. Phys. Lett.* **1970**, *6*, 207−210.

(26) Yang, M.; Fleming, G. R. *Chem. Phys.* **2002**, *275*, 355−372.

(27) Davydov, A. S. *Sov. Phys. Usp* **1964**, *7*, 145.

(28) Mohseni, S. L.; Masoud. *New J. Phys.* **2010**, *12*, 75020.

(29) Engel, E.; Leo, K.; Hoffmann, M. *Chem. Phys.* **2006**, *325*, 170−177.

(30) Tamai, Y.; Matsuura, Y.; Ohkita, H.; Benten, H.; Ito, S. *J. Phys. Chem. Lett.* **2014**, *5*, 399−403.

(31) Yoshikawa, K.; Matsuda, K.; Kanemitsu, Y. *J. Phys. Chem. C* **2010**, *114*, 4353−4356.

(32) Lüer, L.; Hoseinkhani, S.; Polli, D.; Crochet, J.; Hertel, T.; Lanzani, G. *Nat. Phys.* **2009**, *5*, 54−58.

(33) Haedler, A. T.; Kreger, K.; Issac, A.; Wittmann, B.; Kivala, M.; Hammer, N.; Kohler, J.; Schmidt, H.-W.; Hildner, R. *Nature* **2015**, *523*, 196−199.

(34) Akselrod, G. M.; Deotare, P. B.; Thompson, N. J.; Lee, J.; Tisdale, W. A.; Baldo, M. A.; Menon, V. M.; Bulović, V. *Nat. Commun.* **2014**, *5*; 10.1038/ncomms4646

(35) Walker, B. J.; Bulović, V.; Bawendi, M. G. *Nano Lett.* **2010**, *10*, 3995−3999.

DOI: 10.1021/acs.nanolett.6b02529
Nano Lett. XXXX, XXX, XXX−XXX

(36) Qiao, Y.; Polzer, F.; Kirmse, H.; Steeg, E.; Kühn, S.; Friede, S.; Kirstein, S.; Rabe, J. P. *ACS Nano* **2015**, *9*, 1552−1560.
(37) Lyon, J. L.; Eisele, D. M.; Kirstein, S.; Rabe, J. P.; Vanden Bout, D. A.; Stevenson, K. J. J. *J. Phys. Chem. C* **2008**, *112*, 1260−1268.

DOI: 10.1021/acs.nanolett.6b02529
Nano Lett. XXXX, XXX, XXX−XXX